J. Mech. Phys. Solids 203 (2025) 106229

Contents lists available at ScienceDirect

Journal of the Mechanics and Physics of Solids

journal homepage: www.elsevier.com/locate/jmps

Nonlinear contact mechanics of soft elastic spheres under extreme compression

Tong Mu [a,b], Ruozhang Li [b,c], Changhong Linghu [b,*], Yanju Liu [d], Jinsong Leng [a,*], Huajian Gao [e], K. Jimmy Hsia [b,f,*]

[a] Centre of Composite Materials and Structures, Harbin Institute of Technology (HIT), Harbin 150080, PR China
[b] School of Mechanical and Aerospace Engineering, Nanyang Technological University, 50 Nanyang Avenue, Singapore 639798, Singapore
[c] State Key Laboratory of Mechanical System and Vibration, School of Mechanical Engineering, Shanghai Jiao Tong University, 800 Dongchuan Road, Shanghai 200240, PR China
[d] Department of Astronautical Science and Mechanics, Harbin Institute of Technology (HIT), Harbin 150080, PR China
[e] Mechano-X Institute, Applied Mechanics Laboratory, Department of Engineering Mechanics, Tsinghua University, Beijing 100084, PR China
[f] School of Chemistry, Chemical Engineering and Biotechnology, Nanyang Technological University, 50 Nanyang Avenue, Singapore 639798, Singapore

ARTICLE INFO

Keywords:
Contact mechanics
Contact nonlinearity
Flattening problem
Large deformation
Analytical models

ABSTRACT

The contact of soft elastic spheres on substrates is a fundamental problem with significant relevance to fields such as bioengineering, robotics, micro-assembly, and wearables. Accurate analytical solutions for contact behaviors under extreme compression, particularly at compression ratios (compression displacement normalized by sphere radius) exceeding 10 %, are still lacking. This study investigates the contact mechanics of an elastic sphere against a rigid substrate (i.e., the flattening problem) under large deformations, integrating theoretical analysis, finite element analysis (FEA) simulations, and experiments. A finite-deformation theory framework for the flattening problem is proposed, accounting for finite-thickness and radial expansion effects. This framework facilitates analytical solutions for contact force, contact radius, and contact pressure. Systematic analysis of the three key sources of nonlinearity—geometry, material, and contact properties—reveals that geometric nonlinearity is the primary factor causing deviations in contact forces from the Hertzian theory. Based on these insights, explicit solutions for contact force, contact radius, and contact pressure are obtained using simple linear correction functions, achieving excellent agreement with FEA results. Experimental validation with Ecoflex samples demonstrates the high accuracy of these solutions at compression ratios up to 80 %. Additionally, their applicability to cellular mechanics is validated through precise predictions of contact forces reported in the literature for various cell types at compression ratios up to 75 %. This work provides an effective approach to addressing nonlinearities in the flattening problem, enabling accurate predictions of contact behavior under extreme compression. Our findings offer valuable guidelines for contact analysis and structural design involving soft elastomers.

* Corresponding authors.
E-mail addresses: ling0090@e.ntu.edu.sg (C. Linghu), lengjs@hit.edu.cn (J. Leng), kjhsia@ntu.edu.sg (K.J. Hsia).

https://doi.org/10.1016/j.jmps.2025.106229
Received 23 February 2025; Received in revised form 12 May 2025; Accepted 3 June 2025
Available online 7 June 2025

1. Introduction

Compression of soft spheres (i.e., the flattening problem) under extreme deformation is a common phenomenon in daily life and engineering, with significant relevance across various fields, including biomechanics, human-machine interactions, and wearable devices. For example, in biomechanics, understanding the response of live cells and tissues under extreme compression is critical for the study of cell and tissue mechanics and morphogenesis (Lulevich et al., 2006; McGarry, 2009; Moeendarbary and Harris, 2014). In the study of human-machine interactions, it is essential to develop adaptive systems capable of performing tasks such as softly touching human body or grasping using soft robotic components (Abondance et al., 2020; Choi et al., 2018; Xydas and Kao, 1999). In wearable devices, flexible yet highly sensitive pressure sensing can only be achieved by accurately modeling the deformation properties of soft materials (Flavin et al., 2024; Tee et al., 2015; Yang et al., 2021; Zhang et al., 2022; Zhu et al., 2024). In other advanced fields such as mechanical meta-surfaces, soft spheres under extreme compression facilitates the creation of surfaces with tunable frictional properties for advanced applications in tribology (Aymard et al., 2024). In smart adhesives, the switchable flattening under large deformation effectively enhances the materials' adhesion capabilities (Li et al., 2024a, 2024b, 2018; Linghu et al., 2023a, 2024, 2023b; Yu et al., 2025; Zhao et al., 2022). In all these applications, accurate and efficient predictions of responses of a soft sphere under extreme compression, such as contact force and contact radius, are fundamental to improving structural designs and optimizing performance.

The basic solution for the contact between two elastic spheres under small deformation was obtained by Hertz (Hertz, 1882), who laid the groundwork for modern contact mechanics. Since then, substantial progress has been made in studying various contact scenarios, particularly for two common cases with direct practical relevance (Ghaednia et al., 2017): the indentation problem, representing contact between a rigid sphere and an elastic substrate, and the flattening problem, involving contact between an elastic sphere and rigid substrates, as illustrated in Fig. 1.

Under small deformation, these two problems are equivalent within the framework of the Hertz theory. Specifically, the relationship between the contact force and the compression ratio, defined as the compressive displacement (δ) normalized by the sphere radius (R), remains identical under the same effective contact radius R and contact modulus E^*. However, as deformation increases, both the flattening and indentation problems deviate from Hertzian theory predictions, as evidenced by the finite element analysis (FEA) results shown in Fig. 1. Compared to the FEA simulation results, the Hertz theory predicts a lower contact pressure for the flattening problem and a higher contact pressure for the indentation problem under a given compression ratio, and the deviation remains even when the ideal spherical profile is considered (Gao et al., 2005; Segedin, 1957; Zheng and Yu, 2007; Zhi-Jun Zheng, 2007).

The nonlinear indentation problem under large deformations has been studied for various applications, including wearable electronics (Leng and Lin, 2011) and drug delivery (Li et al., 2024c), and under various conditions such as non-adhesive contact (Du et al., 2023; Guo et al., 2020), adhesive contact (Chen and Gao, 2007), elastoplastic contact (Moore et al., 2010), piercing (Fakhouri et al., 2015; Fregonese and Bacca, 2021), wrinkle substrates (Zhang, 2023), frictional effects (Hui et al., 2021), elastocapillarity (Shi et al., 2022), finite-thickness substrates (Chen and Chen, 2013), and nano-scale structures (Mo et al., 2009; Xiao et al., 2023; Zhu et al., 2025). The behavior of soft spheres under extreme compression, however, is yet to be fully understood. Experimental and FEA results

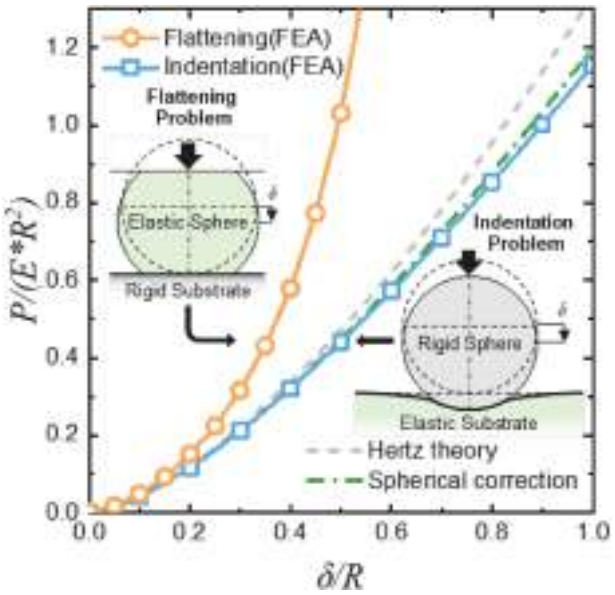

Fig. 1. Results of the contact forces predicted by the Hertz theory (grey dashed line) and its correction considering ideal spherical profile (green dash-dotted line) for the general contact of elastic spheres, and by FEA simulations on the flattening problem (rigid surfaces compressing an elastic sphere in between, orange circles) and the indentation problem (contact between a rigid sphere and an elastic substrate, blue squares) under large deformation ($R = 1$ mm, $E^* = 1$ MPa).

indicate that a power-law solution with a variable exponent may be used to characterize the contact forces within specific range of compression ratios (Lachhab and Weill, 1999; Liu et al., 1998; Tatara, 1991; Xydas and Kao, 1999). Nevertheless, different power-law exponents apparently needed for different compression ratios. A quantitative determination of the value of the power-law exponent remains challenging. By incorporating rubber elasticity and lateral expansion effects under small deformation, Tatara's model (Tatara, 1991) provides a good fit to the experimental results for a relatively stiff carbon black filled rubber sphere under large deformations. However, this model involves five equations to determine its key parameters implicitly. Solving these nonlinear equations requires specifically developed numerical methods (Liu et al., 1998; Tatara et al., 1991). Furthermore, the accuracy of the model strongly depends on the material (Liu et al., 1998).

In the current study, we investigate the problem of a soft sphere under extreme compression (a.k.a., the flattening problem) through an integrated theoretical analysis, FEA simulations, and experimental measurement approach. The primary objectives are to identify the key factors affecting the nonlinear behavior and to obtain an analytical solution for the flattening sphere problem under large deformation. To enhance practical usability, explicit expressions approximating the analytical solutions for key contact variables—contact force, contact radius and contact pressure—are derived. Predictions of the approximate expressions are validated against the FEA simulations and experimental tests. Finally, the applicability of the proposed model is demonstrated by its accurate predictions of the compression forces measured during compression of various types of live cells.

2. A brief review of Hertz theory

In 1882, Hertz established the classical theory for the contact between two elastic spheres (or ellipsoids in general) (Hertz, 1882),

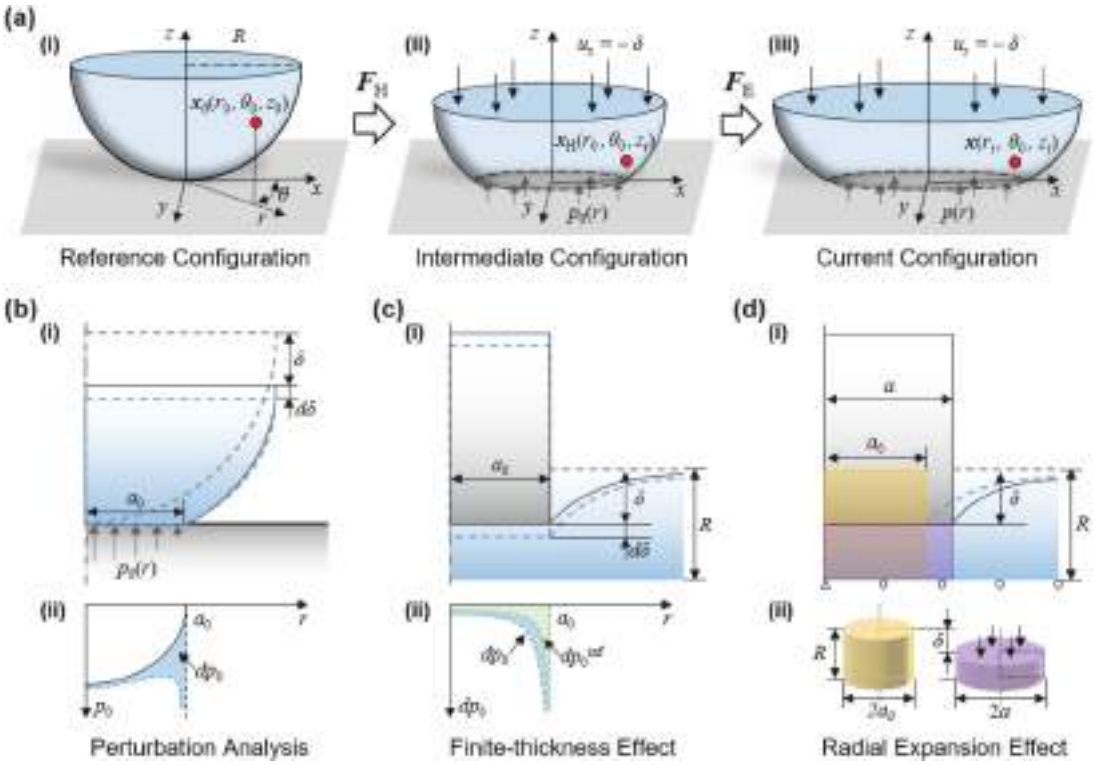

Fig. 2. Schematics showing the mechanics model of the flattening problem. (**a**) Configurations of a flattening hemisphere under a large-compression deformation considering vertical flattening and radial expansion separately. (i) Reference configuration. (ii) Intermediate configuration. (iii) Current configuration. The contact pressure at the contact surface ($z = 0$) is denoted as $p_0(r)$ and $p(r)$ in the intermediate and current configurations, respectively. (**b-d**) **Infinitesimal increment of the flattening problem under large deformation.** (**b**) A model of the flattened hemisphere in the intermediate configuration. (i) Schematics of the hemisphere compressed under a displacement δ. The grey dash line denotes the undeformed configuration of the hemisphere, and the blue dash line denotes the configuration under a displacement increment $d\delta$. (ii) Illustration of the contact pressure distribution under a press-in displacement δ (black solid line) and distribution with a displacement increment $d\delta$ (blue dash line). The variation of the contact pressure dp_0 (blue area) is equivalent to that in the indentation model of a rigid flat punch on an elastic substrate under a displacement increment $d\delta$ with a press-in displacement of δ. (**c**) Consideration of the finite-thickness effect in the flat punch indentation model. (i) Illustration of the contact between a rigid flat punch with a radius a_0 and an elastic substrate with a thickness R. (ii) Illustration of the contact pressure distribution caused by press-in displacement increment $d\delta$ of the flat punch with a pre-compression displacement δ (blue dash curve with blue area). (**d**) Consideration of the expansion of the contact radius a under a displacement increment $d\delta$. (i) Illustration of the contact between a rigid flat punch with a radius a and an elastic substrate. (ii) Illustration showing the cylinder region (yellow region) compressed into the flattened cylinder region (purple region) under a large uniaxial compression δ.

where the mechanics solution involves the effective contact radius $R = 1/(1/R_1 + 1/R_2)$ and the effective contact modulus $E^* = /[(1 - \nu_1^2)/E_1 + (1 - \nu_2^2)/E_2]$, where R_1, ν_1, and E_1 represent the radius, Poisson's ratio and modulus of one contacting sphere, and R_2, ν_2, and E_2 of the other. Hertz theory primarily focuses on local stress distribution in the contact region, neglecting the influence of the far-field stress distribution. Consequently, if focusing on the contact region only, the flattening problem can be approximated by the Hertz theory when the radius R_1 and modulus E_1 of one sphere approaches infinity, (i.e., the contact between an elastic sphere and a rigid substrate).

In the Hertz theory, the pressure distribution within the contact region is

$$p_{\mathrm{H}} = \frac{3}{2}\bar{p}_{\mathrm{H}}\sqrt{1 - \frac{r^2}{a_{\mathrm{H}}^2}},\ (r \le a_{\mathrm{H}}), \tag{1}$$

where a_{H} is the contact radius and $\bar{p}_{\mathrm{H}}$ is the average contact pressure in the contact area:

$$a_{\mathrm{H}} = \sqrt{R\delta}, \tag{2}$$

$$\bar{p}_{\mathrm{H}} = \frac{4}{3\pi}\frac{E^* a_{\mathrm{H}}}{R}. \tag{3}$$

The vertical displacement on the contact surface satisfies the geometric relationship as

$$u_z = -\frac{r^2}{2R},\ (r \le a_{\mathrm{H}}) \tag{4}$$

The contact force corresponds to the integral of the contact pressure given by Eq. (1) over the whole contact area:

$$P_{\mathrm{H}} = \frac{4}{3}E^* R^2 \left(\frac{\delta}{R}\right)^{3/2}, \tag{5}$$

where $E^* = E/(1 - \nu^2)$, E is the Young's modulus and ν the Poisson's ratio of the elastic sphere.

3. Modeling of the flattening problem under large deformation

3.1. Finite-deformation framework of the flattening problem

Due to the symmetry of the flattening problem (as shown in the inset in Fig. 1), it can be modeled as the problem of contact between an elastic hemisphere and a rigid substrate (Fig. 2a). In this setup, a vertical displacement is applied to the upper surface of the hemisphere, with no shear stress present. To model the flattening problem under large deformation, we use a cylindrical coordinate system, in which z as the axis of symmetry with its origin at the center of the contact area, as illustrated in Fig. 2a. A point in the reference configuration located at $\boldsymbol{x}_0 = (r_0, \theta_0, z_0)$ (see Fig. 2a-i) maps onto its current position $\boldsymbol{x} = (r_t, \theta_0, z_t)$ at time t after deformation (Fig. 2a-iii). To analyze the flattening and the radial expansion of flattened sphere, we introduce an artificial intermediate configuration including only the vertical flattening effect (Fig. 2a-ii). From the reference configuration to the intermediate configuration, the point $\boldsymbol{x}_0$ moves to $\boldsymbol{x}_{\mathrm{H}} = (r_0, \theta_0, z_t)$ vertically. Since the radial coordinate remains fixed, the displacement of the contact surface in the intermediate configuration follows the geometric relationship given by the Hertz theory (Eq. (4)). We call the deformation gradient between the reference configuration and the intermediate configuration as the Hertzian deformation gradient $\boldsymbol{F}_{\mathrm{H}}$ here.

The total deformation gradient $\boldsymbol{F}$, the Hertzian deformation gradient $\boldsymbol{F}_{\mathrm{H}}$, and the radial expansion deformation gradient $\boldsymbol{F}_{\mathrm{E}}$ are defined as:

$$\boldsymbol{F} = \frac{\partial \boldsymbol{x}}{\partial \boldsymbol{x}_0}, \tag{6}$$

$$\boldsymbol{F}_{\mathrm{H}} = \frac{\partial \boldsymbol{x}_{\mathrm{H}}}{\partial \boldsymbol{x}_0}, \tag{7}$$

$$\boldsymbol{F}_{\mathrm{E}} = \frac{\partial \boldsymbol{x}}{\partial \boldsymbol{x}_{\mathrm{H}}}, \tag{8}$$

and they have the relationship as:

$$\boldsymbol{F} = \boldsymbol{F}_{\mathrm{E}} \cdot \boldsymbol{F}_{\mathrm{H}}. \tag{9}$$

The determinant of the total deformation gradient,

$$J = \det \boldsymbol{F}, \tag{10}$$

corresponds to the volumetric deformation.

The volumetric deformation is only considered in the radial expansion step. Thus, the determinants of deformation gradients of each step are given by:

$$\det \boldsymbol{F}_{\mathrm{E}} = J,\ \det \boldsymbol{F}_{\mathrm{H}} = 1. \tag{11}$$

To analyze the contact stress, the first Piola-Kirchhoff (PK-1) stress $\boldsymbol{T}$, which represents the stress of a unit undeformed area, is introduced in the intermediate configuration.

There is a transformation relationship between PK-1 stress $\boldsymbol{T}$ in the intermediate configuration and the Cauchy stress $\boldsymbol{\sigma}$ in the current configuration, as follows:

$$\boldsymbol{T} = J\boldsymbol{\sigma} \cdot \boldsymbol{F}_{\mathrm{E}}^{-T}. \tag{12}$$

Under compression, the contact radius is denoted as a in the current configuration and a_0 in intermediate configuration. The relationship between a and a_0 can be given by:

$$a = \int_0^{a_0} \lambda_{rr}(r) dr, \tag{13}$$

where λ_{rr} is the radial stretch of the expansion deformation gradient $\boldsymbol{F}_{\mathrm{E}}$.

The contact pressure is equal to the Cauchy stress on the contact surface:

$$p(r) = -\sigma_{zz}(r, \theta_0, 0),\ (r < a), \tag{14}$$

and the contact pressure of a unit area in the intermediate configuration is determined by PK-1 stress $\boldsymbol{T}$:

$$p_0(r) = -T_{zz}(r, \theta_0, 0),\ (r < a_0). \tag{15}$$

Then the total contact force can be calculated from Eq. (14) or Eq. (15) as:

$$P = \int_0^{a} p(r) 2\pi r dr = \int_0^{a_0} p_0(r) 2\pi r dr. \tag{16}$$

3.2. Incremental analysis under intermediate configuration

Considering the contact process with a gradual increase in the contact force P starting from zero, the current value of the contact force can be expressed as the integral of the incremental force:

$$P = \int_0^{P} d\widetilde{P} = \int_0^{a_0} \frac{d\widetilde{P}}{d\widetilde{\delta}} d\widetilde{\delta} = \int_0^{a_0} \frac{d\widetilde{P}}{d\widetilde{\delta}} \frac{d\widetilde{\delta}}{d\widetilde{a}_0} d\widetilde{a}_0, \tag{17}$$

where $\widetilde{\delta}, \widetilde{P}, \widetilde{a}_0$ denote the displacement, contact force, and contact radius of each increment in integrals. The contact stiffness, $dP/d\delta$, represents the increment of contact force dP due to an increment of compression displacement $d\delta$ under a given contact radius a_0, as shown in Fig. 2b

The increment of contact force dP can be obtained by the integration of the variation of the contact pressure dp_0 over the contact area, as:

$$dP = \int_0^{a_0} dp_0(r_0) 2\pi r_0 dr_0. \tag{18}$$

According to (Sneddon, 1965) and (Popov et al., 2019), the variation in contact pressure dp_0 in the spherical contact problem under a small displacement increment of $d\delta$ is equal to the change in contact pressure distribution between a flat-punch of radius a_0 and an elastic substrate composed of the same material as the elastic sphere under a displacement increment $d\delta$ with a press-in displacement of δ, as illustrated in Fig. 2c.

For a flat punch indentation system with an elastic substrate of infinite thickness, the variation of the pressure distribution is given as (Popov et al., 2019):

$$dp_0^{\mathrm{inf}}(r_0) = \frac{E^*}{\pi} \frac{1}{\sqrt{a_0^2 - r_0^2}} d\delta. \tag{19}$$

However, the thickness effect of the substrate is non-negligible under large deformation. A correction of finite thickness effect is required to modify Eq. (19):

$$dp_0(r_0) = \chi\left(\frac{\delta}{R}\right) \cdot \frac{E^*}{\pi} \frac{1}{\sqrt{a_0^2 - r_0^2}} d\delta, \tag{20}$$

where χ is the correction function, which represents the geometric nonlinearity effect caused by the large compressive deformation of the finite-thickness substrate.

Flattening of the cylindrical region of the substrate under the flat punch is the main source of the nonlinearity, as shown in Fig. 2d Therefore, the specific form of χ can be determined by considering the uniaxial compression of this cylindrical region under large deformations.

According to Eq. (12), the PK-1 stress is equal to the negative value of the contact pressure, i.e., $T = T_{zz} = -p_0$. Therefore, the correction to the pressure (Eq. (20)) is equivalent to the correction to the PK-1 stress in the cylinder, given by:

$$T = \chi \cdot T_{\text{linear}}, \tag{21}$$

where T_{linear} is the linear form of compression force under the uniaxial compression given as:

$$T_{\text{linear}} = -E\frac{\delta}{R}. \tag{22}$$

Since the PK-1 stress T is also a function of compression ratio $\delta/R = 1 - \lambda$, the correction function is therefore determined by:

$$\chi\left(\frac{\delta}{R}\right) = \frac{T\left(\frac{\delta}{R}\right)}{T_{\text{linear}}\left(\frac{\delta}{R}\right)}. \tag{23}$$

The correction function χ represents the nonlinearity of the large deformation in the flattening problem, originating from geometric and/or material nonlinearity. Eq. (23) does not have an explicit expression in general. However, for typical hyperelastic materials using various elastomeric constitutive relationships (see details in Section 6.2), an approximate form can be obtained using a hyperelastic model (e.g., the Neo-Hookean model).

Utilizing the correction function of the pressure variation (Eq. (20)) for a small increment, the contact force can be derived according to a series of integrations and expressed as the product of the correction function and the Hertzian contact force (see Appendix A for the details):

$$P = \chi\left(\frac{\delta}{R}\right) P_{\text{H}}. \tag{24}$$

3.3. Radial expansion effect

As shown in Fig. 2d, the radial expansion of the substrate under the punch in every displacement increment can be determined by uniaxial compression of a cylinder of radius $\widetilde{a}_0$, which increases from 0 to the final contact radius a_0. The radial stretch of the cylinder is $\lambda_{rr} = \sqrt{J/\lambda}$ in every increment, thus the total expansion can be obtained from Eq. (13) as:

$$a = \int_0^{a_0} \sqrt{\frac{J}{\lambda}} d\widetilde{a}_0 = \int_0^{a_0} \sqrt{\frac{J}{1 - \frac{\delta - \delta(\widetilde{a}_0)}{R}}} d\widetilde{a}_0. \tag{25}$$

For incompressible materials ($J = 1$), the contact radius is given by an explicit expression as:

$$a_{\text{IC}} = R\text{arctanh}\sqrt{\delta/R}, \tag{26}$$

where the inverse hyperbolic tangent function $\text{arctanh}x = \frac{1}{2}\ln\frac{1+x}{1-x}$.

The contact radius for incompressible materials can then be expressed as a function of the Hertzian contact radius (given by Eq. (2)) in the following form:

$$a_{\text{IC}} = R\text{arctanh}\frac{a_{\text{H}}}{R}. \tag{27}$$

Obtaining an analytical solution for the contact radius for compressible materials is difficult. However, a semi-empirical solution for a range of Poisson's ratios can be obtained by fitting the FEA results, as will be discussed in Section 6.4.

According to Eq. (20), the distribution of contact pressure under the intermediate configuration can be calculated as:

$$p_0(r_0) = \int_{\delta^{-1}(r_0)}^{\delta} dp_0 = \frac{2\chi E^*}{\pi R}\sqrt{a_0^2 - r_0^2}, \ (r_0 \le a_0). \tag{28}$$

Assuming uniform expansion, a point on the contact surface in the intermediate configuration can be mapped onto the current configuration as:

$$\frac{r}{r_0} = \frac{a}{a_0}. \tag{29}$$

Thus, the contact pressure in the current configuration can be calculated by Eqs. (12), (14) and (15) as:

$$p = \left(\frac{a_0}{a}\right)^2 p_0 = \frac{3}{2}\bar{p}\sqrt{a^2 - r^2},\ (r \le a), \tag{30}$$

where the average pressure in the current configuration is:

$$\bar{p} = \frac{4}{3\pi}\frac{\chi E^* a_0}{R}\left(\frac{a_0}{a}\right)^2. \tag{31}$$

It is interesting to note from Eq. (1) and Eq. (30) that the distribution of contact pressure still takes the form of the Hertzian solution, albeit the contact radius (Eq. (25)) and average pressure (Eq. (31)) is larger than the Hertzian contact radius (Eq. (2)) and the Hertzian contact pressure (Eq. (3)), respectively.

4. FEA setup

We carry out the FEA simulations to validate the analytical solution of the contact pressure and to obtain the semi-empirical expressions of the contact radius and pressure for hyperelastic materials.

Axisymmetric FEA model was constructed in ABAQUS (Dassault Systèmes, 2023), as shown in Fig. 3a, in which an elastic hemisphere of radius $R = 1$ mm is brought into contact with a rigid plane. The displacement boundary condition with a maximum value of 0.5 mm is applied on the top of the hemisphere. The contact between the elastic body and the rigid surface is achieved using the node-to-surface method, with contact property specified as either frictionless or rough.

The analysis consists of two steps: the top of the hemisphere is first compressed downward by 0.01 mm with the time increment automatically calculated; the displacement is then increased from 0.01 mm to 0.5 mm, with a 0.01 mm incremental for each step. The FEA mesh consists of 9753, 4-node axisymmetric quadrilateral elements (CAX4H elements) (see Fig. 3b). The hybrid formulation (see ABAQUS Manual, Theory, Elements) is used (Dassault Systèmes, 2023). The maximum edge length of the elements does not exceed 0.0154 mm, and the aspect ratio does not exceed 2.25. No element distortion occurred even under extreme compression ($\delta/R = 0.5$), as shown in Figs. 3b-ii, iii. The mesh convergence analysis shows that reducing the mesh size by a factor of 2 results in a total contact force difference of <0.3 %.

Three typical constitutive models of elastomers are used, including the linear elastic model, the neo-Hookean model, and the Arruda-Boyce model (Arruda and Boyce, 1993). The neo-Hookean and the Arruda-Boyce models are consistent with the linear elastic model under small deformations. The shear modulus μ of the linear elastic model is fixed at 1 MPa, and Poisson's ratio ν varies from 0.3 to 0.5, covering the typical range of common soft elastomers (Mott et al., 2008; Theocaris, 1969). The material parameters of the neo-Hookean model and their corresponding relationships with the linear elastic model are given in Appendix B. In the Arruda-Boyce model, in addition to the shear modulus μ and compressibility parameter $D_0 = 2/\kappa$ (κ is the bulk modulus), we also choose a locking stretch $\lambda_m = 5$, which is a typical value for rubber-like material (Arruda and Boyce, 1993), and the influence of the locking stretch λ_m is further examined in Appendix C.

Different contact properties are considered in the FEA simulations to evaluate their influence on the contact behaviors of the flattening problem. A surface-to-surface contact is set between the elastic sphere and the rigid substrate using the node-to-surface discretization method. The contact properties between the surfaces include normal behavior and tangential behavior: The normal behavior is defined as "Hard" contact, while the tangential direction is either frictionless or no sliding.

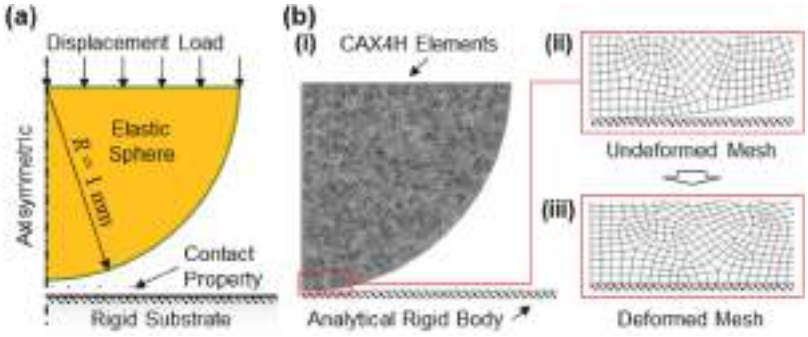

Fig. 3. FEA simulation setup for the flattening problem. (**a**) Schematics showing the geometry, applied load, and boundary conditions. The contact system consists of an elastic hemisphere and a fixed rigid substrate (modeled as an analytical rigid body). A vertical displacement is applied on the top surface of the hemisphere. (**b**) Meshing configuration of the elastic hemisphere, illustrating the discretization used in the analysis. (i) Mesh of the whole system. (ii) Magnified views of the mesh of the contact region under undeformed state and (iii) deformed state ($\delta/R = 0.5$), where no element distortion occurred.

5. Experimental setup

To validate the analytical solution experimentally, we conducted compression tests using Ecoflex 00-30 (Smooth-On Inc., see Appendix D for details of the sample preparation). Figs. 4a-b illustrate the setup for the compression tests of elastic spheres. Two clean glass slides were used as flat rigid substrates. The lower substrate was glued on a platform, while the upper substrate was connected to a load cell through a leveler. Upon adjusting the leveler to ensure the top and bottom slides were parallel, an Ecoflex 00-30 sphere was placed on the lower substrate. Before testing, it was verified that the upper substrate makes normal contact with the elastic sphere. The compression rate was 0.1 mm/s, with typical deformed configurations shown in Fig. 4c. Each compression test was repeated three times using different samples.

6. Results and discussion

6.1. Nonlinearity of the flattening problem

In the flattening problem, three sources of nonlinearity exist: geometric, material, and contact boundary-condition nonlinearities. They all potentially contribute to the discrepancies between the FEA simulation results and the Hertz theory predictions based on linear elasticity (as shown in Fig. 1). This sub-section examines these nonlinearities individually using FEA simulations.

Material nonlinearity. To evaluate the influence of material nonlinearity, we consider two hyperelastic models (see details in Appendix B). One is the neo-Hookean model, a direct extension of the linear elastic model, which has two material parameters, the shear modulus and Poisson's ratio (Boyce and Arruda, 2000). Despite its simplicity, the neo-Hookean model demonstrates excellent accuracy in describing the mechanical behavior of elastomers, such as rubbers (Boyce and Arruda, 2000; Treloar, 1975), hydrogels (Hong et al., 2009; Huang et al., 2020), and rubber-state shape memory polymers (SMPs) (Chen and Lagoudas, 2008; Diani et al., 2006; Huang et al., 2020). The other is the Arruda-Boyce model (Arruda and Boyce, 1993), or eight-chain model, derived from a molecular physics framework. This model provides accurate predictions across a wide deformation range for elastomers, with its validity demonstrated in rubbers (Arruda and Boyce, 1993), SMPs (Nguyen et al., 2008), and hydrogels (You et al., 2023).

Fig. 5a shows the contact forces obtained from FEA simulations using different constitutive models with the same initial shear modulus. The linear elastic, neo-Hookean and Arruda-Boyce models all yield very similar results, deviating from the predictions of the Hertz theory for compression ratio larger than 10 %. Further investigation (see details in Appendix C) shows that the contact behavior of common elastomeric materials, including rubbers, hydrogels, and SMPs, is insensitive to the parameters of the constitutive models. These findings suggest that material nonlinearity has minimal impact on the flattening problem of elastomers.

To investigate the origin of the similarity among different materials, the inset in Fig. 5a presents the compressive stress-strain curves for various constitutive models. As shown, the curves are nearly identical within the true strain between 0 and −1, indicating limited influence of the material nonlinearity under this level of deformation. Furthermore, it is found from the FEA results (see details in Appendix E) that the absolute value of the maximum (compressive) true strain in the flattening system is smaller than 1 under a compression ratio up to $\delta/R = 0.5$, using either the neo-Hookean model or the Arruda-Boyce model. Therefore, even though the

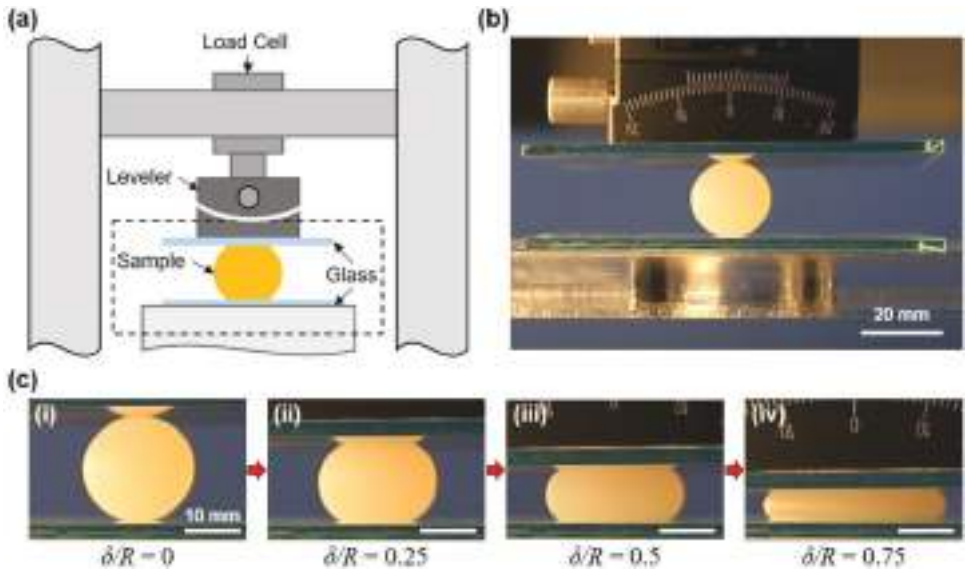

Fig. 4. Experimental test setup for the flattening problem using an Ecoflex sphere. (**a**) Schematic of the compression test setup, showing the elastic sphere (Ecoflex 00-30, radius 10 mm) positioned between two glass substrates. The lower substrate is fixed, while the upper substrate is connected to a load cell via a leveler. (**b**) Close-up photograph of the experimental setup, highlighting the elastic sphere in its undeformed state. (**c**) Snapshots of the elastic sphere under various compression displacements: (i) $\delta/R = 0$, (ii) $\delta/R = 0.25$, (iii) $\delta/R = 0.5$, and (iv) $\delta/R = 0.75$.

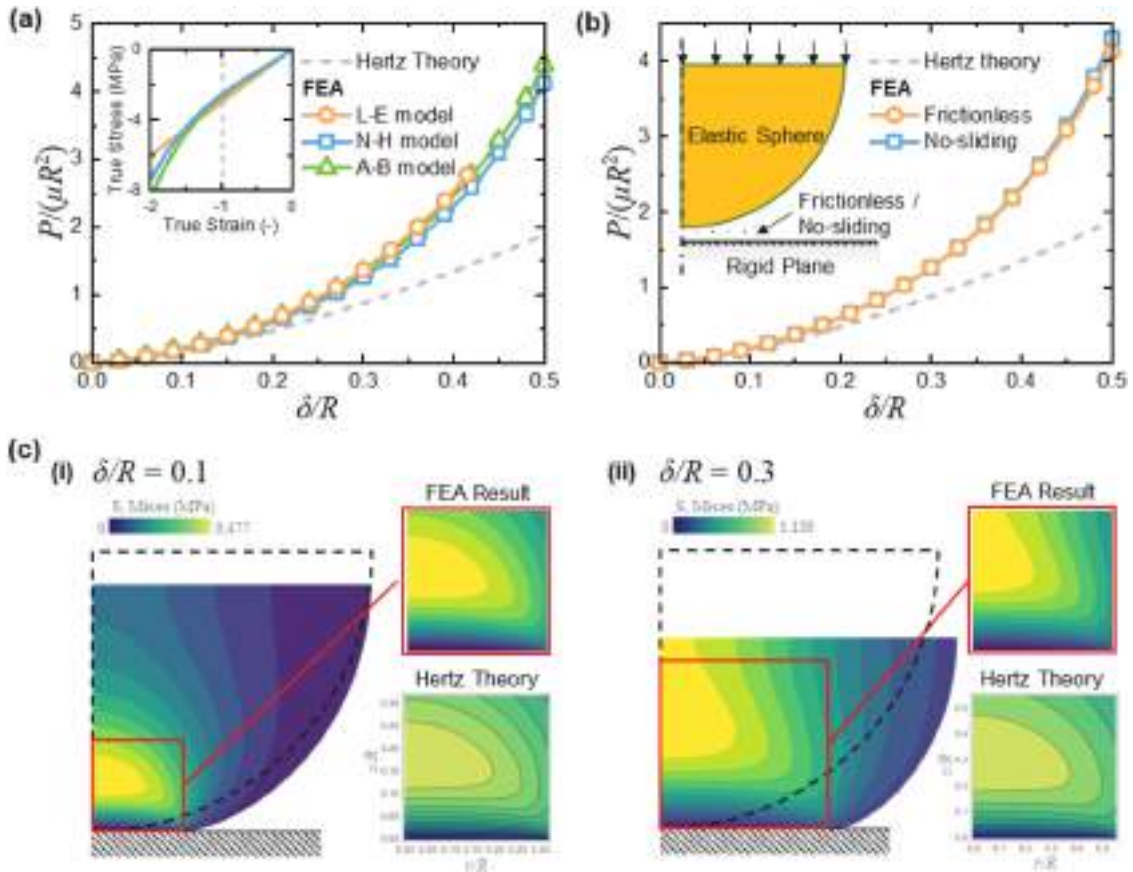

Fig. 5. Analysis of the nonlinearity effects in the flattening problem. (**a**) Effect of the material nonlinearity on the contact force. The grey dash line represents predictions from Hertz theory, while the lines with scattered points show FEA results for different constitutive models (orange circles: linear elastic (L-E) model, blue squares: neo-Hookean (N-H) model, green triangles: Arruda-Boyce (A-B) model). The inset shows the stress-strain curve under uniaxial compression for each constitutive model. (**b**) Influence of the contact conditions on the contact force. FEA results are presented for frictionless (orange circles) and no-sliding (blue squares) conditions, alongside the Hertz theory prediction (grey dashed line). (**c**) Von Mises stress distributions in the elastic sphere under (i) a small compression ($\delta/R = 0.1$) and (ii) a large compression ($\delta/R = 0.3$). Magnified views highlight the stress distribution near the contact region, as compared to predictions from Hertz theory. For a relatively small deformation (e.g., $\delta/R = 0.1$), FEA results show good agreement with Hertz theory. However, for a relatively large compressive deformation (e.g., $\delta/R = 0.3$), significant deviations of FEA results from the Hertz theory are observed, indicating the geometric nonlinearities strongly influence the stress distribution in the flattening problem. (Sphere radius $R = 1$ mm).

sphere is severely flattened, the mechanical behavior predicted by different material models remains similar. The neo-Hookean model is thus used as a representative model below.

Contact boundary properties nonlinearity. We consider two extreme cases: frictionless or no-sliding contact. Fig. 5b shows that the contact forces obtained from the FEA simulations under these two contact conditions are nearly identical, indicating that the contact properties have minimal influence on the flattening problem.

The stress distributions obtained from FEA simulations under small deformation ($\delta/R = 0.1$) and relatively large deformation ($\delta/R = 0.3$) are depicted in Fig. 5c. Under small deformation, the stress distribution agrees well with the prediction from the Hertz theory. However, under large deformation, the stress distribution deviates from the Hertzian prediction. Since Hertz theory is based on the small deformation assumption, its stress distribution ($s/p_{0,\mathrm{H}}$ plotted as a function of r/a_{H} and z/a_{H}) remains unchanged for different compression ratios. The Hertz model, which neglects radial expansion of the contact surface, becomes invalid under large deformations (see Fig. 5c ii). Incorporating geometric nonlinearity into the analysis of the flattening problem is thus critical to obtaining accurate solutions under large deformation.

The above analysis shows that, for a wide range of common polymers, the effects of material nonlinearity and contact boundary property nonlinearity on the flattening problem are negligible. The geometric nonlinearity plays a dominant role in the contact mechanics. Consequently, Hertz theory must be modified to account for geometric nonlinearity for large-deformation scenarios.

6.2. The correction function

Based on the results in the previous sub-section, we use the neo-Hookean model and frictionless contact here in the determination and validation of the correction function for flattening problems.

Uniaxial tension/compression force per unit area, or the PK-1 traction, is obtained from derivative of Helmholtz free energy of neo-Hookean material (detail in Appendix B) as:

$$T_i = \frac{\partial \psi}{\partial \lambda_i} = \frac{2\mu}{3}\left(\lambda_i - \frac{J}{\lambda_i^2}\right) + \kappa \frac{J(J-1)}{\lambda_i}, \ (i = 1,\ 2,\ 3) \tag{32}$$

The PK-1 traction on the radial directions is equal to zero, $T_2 = T_3 = 0$, and Eq. (32) ($i = 2, 3$) is reduced to:

$$\mu J - \mu\lambda_1^3 - 3\kappa J^{\frac{5}{3}}\lambda_1 + 3\kappa J^{\frac{8}{3}}\lambda_1 = 0 \tag{33}$$

The determinant J is determined under a given stretch of $\lambda_1 = 1 - \delta/R$ by Eq. (33), and then substitute the result of J into Eq. (32) ($i = 1$), the compression force $T = T_1$ can be obtained.

The compression force T of neo-Hookean materials does not have an explicit solution in general. However, when the material is incompressible, an explicit solution of the PK-1 traction can be obtained as:

$$T_{\mathrm{IC}} = T_1 = \frac{E}{3}\left(\lambda_1 - \frac{1}{\lambda_1^2}\right). \tag{34}$$

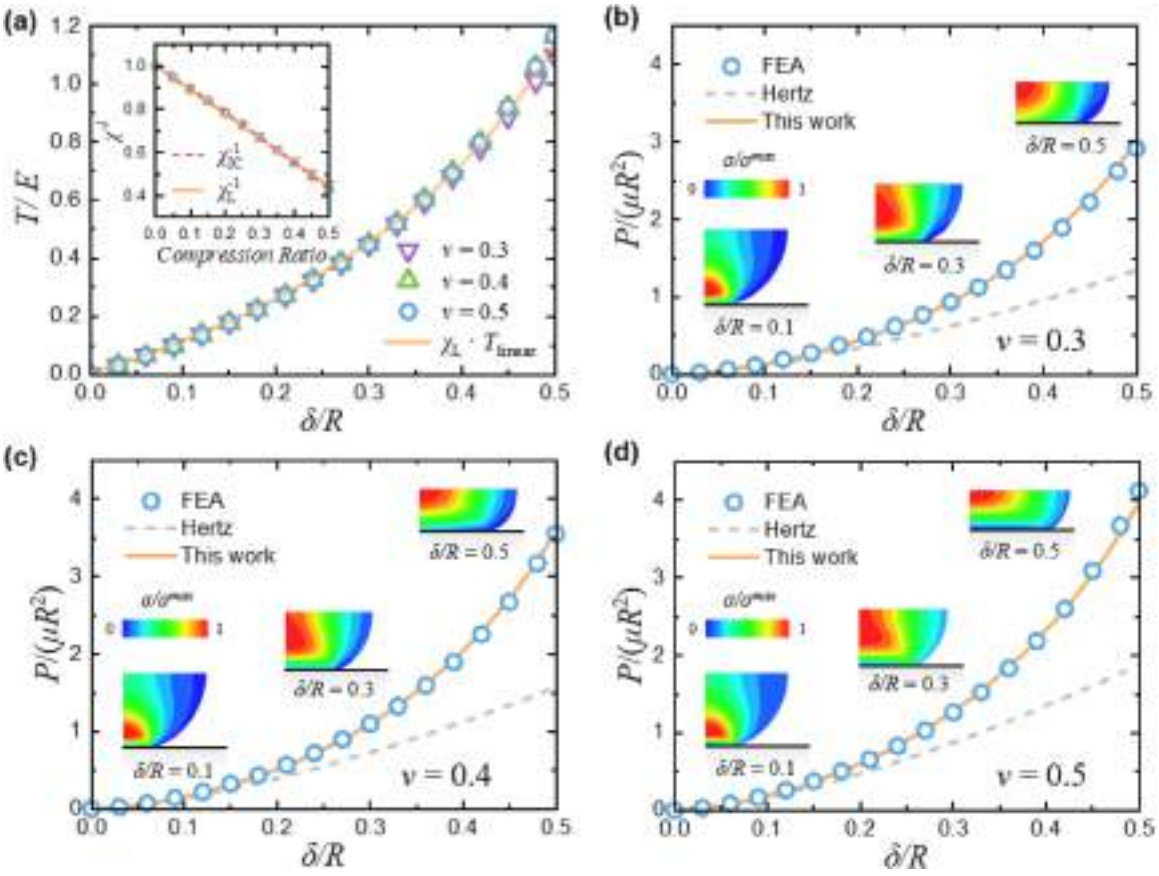

Fig. 6. Determination of correction function and prediction of the contact force with different Poisson's ratios. (**a**) Compression force of cylinders with different Poisson's ratio under uniaxial compression and the prediction using the correction function. Inset shows the reciprocal of the correction function χ, defined as the ratio of actual compression force T to linear form compression force T_{linear}. Results of T_{linear}/T with Poisson's ratio of 0.3 (purple inverted triangles), 0.4 (green triangles), 0.5 (blue circles) are fitted by a universal function with linear form (orange line) in the inset. Cylinders used for these calculations are of same section area A (1 mm^2) and Young's modulus E (1 MPa). (**b**) Comparison of predicted contact force versus compression displacement curves for the flattening problem obtained from the proposed model (this work, orange solid line) and Hertz theory (gray dashed line), validated against the FEA results for Poisson's ratios of (**b**) 0.3, (**c**) 0.4, and (**d**) 0.5. ($R = 1$ mm, $\mu = 1$ MPa in the FEA simulations).

Substitute $\lambda_1 = 1 - \delta/R$ into Eq. (34), the PK-1 traction under uniaxial compression is expressed in term of the compression ratio δ/R, as:

$$T_{\mathrm{IC}} = -E \cdot \frac{\frac{\delta}{R} - \left(\frac{\delta}{R}\right)^2 + \frac{1}{3}\left(\frac{\delta}{R}\right)^3}{\left(1 - \frac{\delta}{R}\right)^2}. \tag{35}$$

The correction function is then determined for incompressible materials according to Eq. (23), as:

$$\chi_{\mathrm{IC}}\left(\frac{\delta}{R}\right) = \frac{1 - \frac{\delta}{R} + \frac{1}{3}\left(\frac{\delta}{R}\right)^2}{\left(1 - \frac{\delta}{R}\right)^2}. \tag{36}$$

Additionally, the correction function can be approximated by a linear form for most practical cases, as:

$$\left[\chi_{\mathrm{L}}\left(\frac{\delta}{R}\right)\right]^{-1} = 1 - k\frac{\delta}{R}, \tag{37}$$

where the fitting parameter $k = 1.114 \approx 10/9$ obtained from least square method gives the coefficient of determination $r^2 > 99.9$ % for compression ratio δ/R between 0 and 0.5. The inset in Fig. 6a demonstrates that the simple expression given by Eq. (37) (orange solid line) is an excellent approximation to the complex expression given in Eq. (36) (red dash line). Eq. (37) shows that the influence of geometric nonlinearity increases rapidly under large compression ratio δ/R. Prediction of the compression force using Eq. (37) is shown in Fig. 6a, which agrees well with the FEA results (blue circles). Additionally, the relationship between contact force and contact radius is then determined by using Eq. (27), and its validity is confirmed Appendix F.

When the neo-Hookean material is compressible, an explicit solution cannot be obtained. Numerical results of the compression force (solved from Eq. (32) and Eq. (33)) of a cylinder with cross-sectional area $A = 1$ mm^2, Young's modulus $E = 1$ MPa and Poisson's ratios of 0.3 and 0.4 under uniaxial compression are also shown in Fig. 6a. Prediction of compression force using Eq. (37) is plotted in Fig. 6a, indicating that the approximation of the correction function, Eq. (37), is able to capture the nonlinear behavior for both impressible and compressible materials of different Poisson's ratios.

6.3. The contact force

Substitute Eq. (37) into Eq. (24), the contact force can be expressed as:

$$F = \frac{F_{\mathrm{H}}}{1 - \frac{10}{9}\frac{\delta}{R}} \tag{38}$$

Figs. 6b-d present the contact force as a function of δ/R in Eq. (38) for the Poisson's ratios ν of 0.3, 0.4, and 0.5. The results demonstrate that the Hertz theory deviates significantly from the FEA results at large deformation for all values of Poisson's ratio, with errors exceeding 30 % at a compression ratio $\delta/R = 0.3$ and >100 % at $\delta/R = 0.5$. For the same range of Poisson's ratios, Eq. (38)

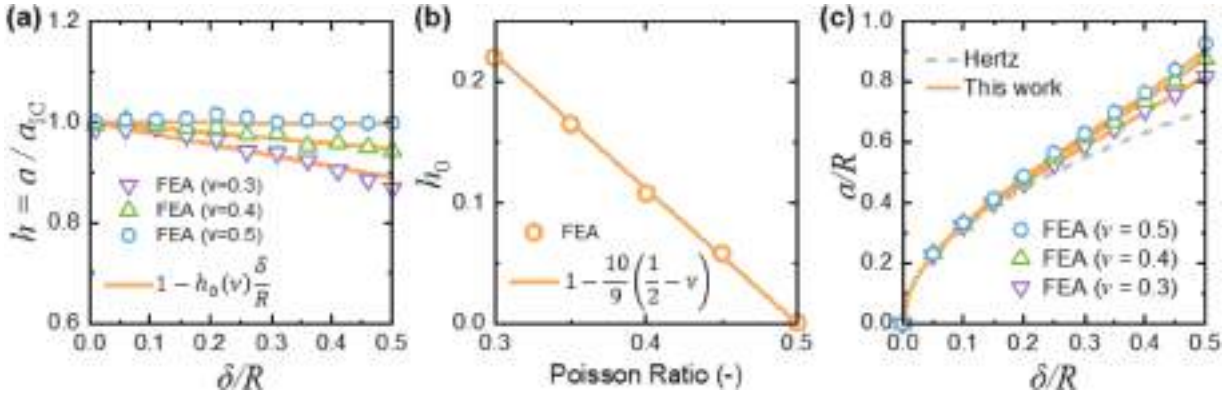

Fig. 7. Determination and validation of the analytical expression for the contact radius. (**a**) Derivation of the correction function for contact radius via linear fitting (orange line) of correction factors obtained from FEA simulations with different Poisson's ratios: 0.3 (purple inverted triangles), 0.4 (green triangles), and 0.5 (blue circles). For a given Poisson's ratio, the contact radius shows a linear relationship with the relative compression δ/R, with the slope h being dependent on the Poisson's ratio. (**b**) Relationship between the slope h of the curves in (**a**) and the Poisson's ratio. A linear fit (orange line) accurately describes this dependency. (**c**) Validation of the proposed analytical expression for the contact radius (orange solid line) against FEA results for Poisson's ratios of 0.3 (purple inverted triangles), 0.4 (green triangles), and 0.5 (blue circles). Hertz theory (gray dashed line) is included for comparison. ($R = 1$ mm, $\mu = 1$ MPa in the FEA simulations).

successfully reduces the maximum error to 5 % across the entire compression range, demonstrating the accuracy of Eq. (37) at predicting the contact force.

Unlike the von Mises stress distributions that remain unchanged predicted by the Hertz theory, the distributions depicted by the insets in Figs. 6b-d illustrate significant evolution at compression ratios δ/R of 0.1, 0.3, and 0.5. The transition of the von Mises stress distribution from Hertzian to non-Hertzian demonstrates that the Hertz theory is no longer accurate for large compression, and the correction function χ must be employed to assess the contact force and stress distribution. It is also noted in the insets in Figs. 6b-d that stress distributions are similar for different Poisson's ratios under the same compression ratio, therefore validating that the correction function χ is independent of Poisson's ratio.

6.4. The contact radius

Since a closed form expression of the contact radius cannot be obtained from Eq. (25) for compressible materials, we establish a semi-empirical expression through fitting FEA results for different Poisson's ratios. Compared to incompressible materials, the contact radius for a compressible material sphere is smaller. Here we introduce an empirical correction function h to approximate the contact radius, a_{IC}, as:

$$a = h \cdot a_{\mathrm{IC}}, \tag{39}$$

where a_{IC} is given by the Hertzian contact radius in Eq. (26).

Fig. 7a illustrates the correction function h calculated using the contact radius a obtained from FEA results. It is noticed that h exhibits a linear relationship with δ/R for a range of Poisson's ratios. Furthermore, since the contact radius a should be consistent with the Hertz prediction a_{H} under small deformation, $h = 1$ when $\delta/R = 0$, the correction function h may be expressed as:

$$h\left(\frac{\delta}{R}, \nu\right) = 1 - h_0(\nu)\frac{\delta}{R}, \tag{40}$$

where h_0 is a function of Poisson's ratio.

Fig. 7b shows the values of h_0 obtained via least-squares fitting for different Poisson's ratios, revealing a linear relationship between h_0 and Poisson's ratio ν:

$$h_0(\nu) = \frac{10}{9}\left(\frac{1}{2} - \nu\right). \tag{41}$$

It is noted that the single fitting parameter 10/9 appears in both the correction function for the contact force (Eq. (38)) and the correction function for the contact radius (Eq. (41)).

Substitute Eq. (40) and Eq. (41) into Eq. (39), we obtain:

$$a = \left[1 - \frac{10}{9}\left(\frac{1}{2} - \nu\right)\frac{\delta}{R}\right] a_{\mathrm{IC}}. \tag{42}$$

Fig. 7c presents the predicted contact radius using Eq. (42). The predictions agree well with the FEA results for different Poisson's ratios. Additionally, the value of the contact radius is higher than those predicted by the Hertz theory, demonstrating that radial expansion is non-negligible in the flattening problem.

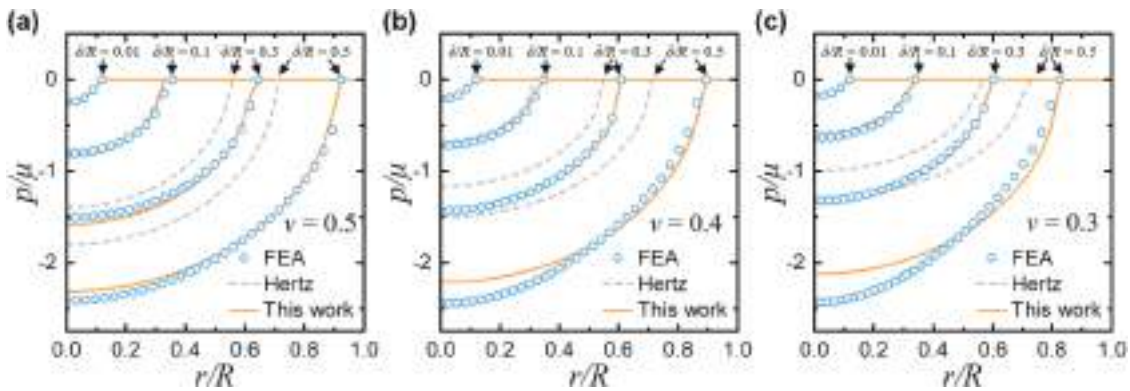

Fig. 8. Validation of the analytical expression for the contact pressure in the proposed model against FEA results. Predictions from proposed model (orange line) are compared with FEA results (blue circles) for different displacement loads (δ/R = 0.01, 0.1, 0.3, and 0.5) under Poisson's ratio of (**a**) 0.5, (**b**) 0.4, and (**c**) 0.3. Hertz theory (gray dashed line) is included for reference. (R = 1 mm, μ = 1 MPa in the FEA simulations).

6.5. The contact pressure

The distribution of contact pressure for compressible materials can be calculated using Eq. (38), Eq. (42), Eq. (30) and Eq. (31). The results for compression ratios of $\delta/R = 0.01$, 0.1, 0.3 and 0.5 are presented in Fig. 8. For compression ratios $\delta/R = 0.01$ and 0.1, the predictions of contact pressure distributions based on the Hertz theory agree well with the FEA results. For large deformation ($\delta/R \geq 0.3$), significant deviation is observed between the Hertzian predictions and the FEA results.

For incompressible materials, i.e., $\nu = 0.5$, Fig. 8a shows that the contact pressure distribution predicted by our model agrees with the FEA results well. For compressible materials, Fig. 8b-c show that our model predictions agree well with the FEA results when $\delta/R \leq 0.3$, but discrepancies are observed at $\delta/R = 0.5$ (the maximum error of 9 % for $\nu = 0.4$ and 12 % for $\nu = 0.3$). These discrepancies suggest that the assumption of self-similar expansion of contact surface (Eq. (29)) may not fully capture the non-uniform radial expansion occurring near the contact center under very large deformation. As a potential improvement, future work could incorporate a mapping between intermediate and current configurations of the contact surface, allowing for a more precise representation of the deformation field and the resulting pressure distribution.

6.6. Experimental validation

We carry out compression experiments using elastomer spheres to validate our model. Details regarding the preparation of experimental samples and the testing procedure are provided in Section 5 and Appendix C.

The modulus of Ecoflex 00-30 exhibits significant variability due to the differences in synthesis conditions (Herren et al., 2020). Consequently, the shear modulus of the elastic sphere was determined by fitting data from the initial stage of the compression tests ($\delta/R \leq 0.1$), where the force-displacement relationship satisfies the Hertz theory (Eq. (5)). A Poisson's ratio of $\nu = 0.5$ is used in the analysis, yielding a shear modulus $\mu = 40.7$ kPa through experimental fitting.

Fig. 9 shows the experimental results of the contact force and contact radius. The maximum compression ratio of the elastomer sphere δ/R was 0.85. The results demonstrate that our analytical solution exhibits strong predictive power for both contact force and contact radius, showing excellent agreement with the experimental measurements. Insets in Fig. 9b depict the shapes of the elastomer sphere at compression ratios of 0.2, 0.5, and 0.8, respectively, demonstrating pronounced radial expansion, leading to increased influence of the geometric nonlinearity.

Fig. 9 also shows the predictions of the Hertz theory and Tatara's model (Tatara, 1991). For small deformation, the Hertz theory and Tatara's model agree well with the experimental data. But at large deformation, the Hertz theory significantly underestimates the contact force and contact radius, while the Tatara model consistently overestimates them, indicating limitations of their applicability.

6.7. Applications in cell mechanics

We have also explored whether our analytical solution can be applied to more complex systems, e.g., indentation of a biological cell. During the compression process, the cell membrane, nucleus, and cytoskeleton all contribute to resisting the contact force, with the cytoskeleton playing a more significant role under large deformation (Lulevich et al., 2006). Since the cytoskeleton is generally regarded as a homogeneous isotropic material (Lulevich et al., 2006; Tartibi et al., 2015), the cell can be approximately treated as a homogeneous elastic sphere under large deformation. Fig. 10 shows the contact forces measured by Tartibi et al. (Tartibi et al., 2015) for human mesenchymal stem cells under three states: live cells ($R = 14.2$ μm, $E^* = 20.8$ kPa), fixed-stained cells ($R = 15.4$ μm, $E^* = 42.2$ MPa. Note: it is known that fixed cells are significantly stiffer than live cells, see, e.g., (Park et al., 2010)), and live-stained cells ($R = 16.3$ μm, $E^* = 22.6$ kPa). The results demonstrate significant nonlinear behaviors under large deformation. Furthermore, the

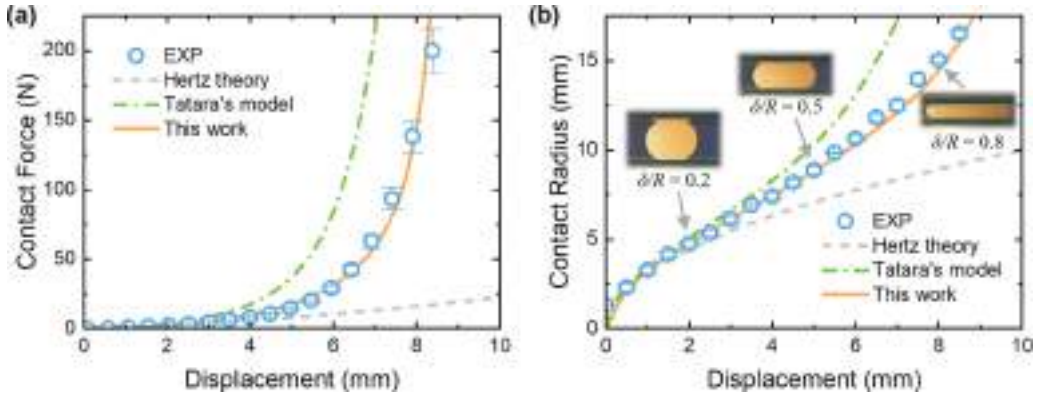

Fig. 9. Experimental validation of the analytical expressions for the (a) contact force and (b) contact radius. (**a**) Comparison of the predicted contact force from the analytical expression (orange solid line) with experimental results (blue dots) using an Ecoflex 00-30 sphere. (**b**) Validation of the analytical expression (orange solid line) for the contact radius against experimental measurements (blue dots) with the same sphere sample. Hertz theory (gray dashed line) and Tatara's model (green dash-dotted line) are also included for comparison.

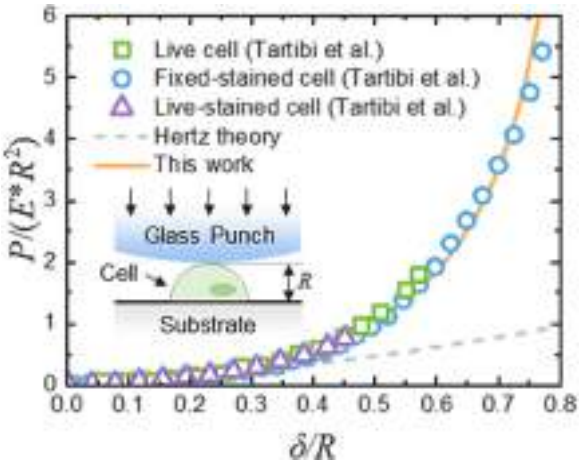

Fig. 10. Prediction of the contact force during the compression of human mesenchymal stem cells under different states. The analytical model's predictions (orange solid line) in this work are compared with experimental data for live cell (green squares), fixed-stained cell (bule circles), and live-stained cell (purple triangles), as reported in (Tartibi et al., 2015). Predictions from Hertz theory (gray dashed line) are also included for comparison.

relationship between the contact force and compression ratio is similar for different cell states. Nevertheless, our analytical solution (Eq. (38)) can successfully capture the cell response under large deformation for all cell states including both live and fixed cells. Our model prediction of the contact force closely matches Tartibi et al.'s experimental measurements, validating our model's capability. This agreement can be attributed to the dominant mechanical response of the cell cytoskeleton in resisting compression, which justifies treating the cell as a continuum elastic body in this regime. Results in Fig. 10 demonstrate our model's utility in addressing mechanics in live cells and potentially other living systems. This method facilitates the analysis of cellular physiological processes under stress conditions, and offers guidance for cell manipulation, including cell transfer technology and 3D bioprinting.

7. Conclusion

In this study, the contact mechanics of an elastic sphere compressed by rigid substrates, commonly referred to as the flattening problem, is investigated using theoretical, FEA simulation, and experimental methods. A theoretical framework for the flattening problem under extreme compression is proposed, accounting for the finite-thickness and radial expansion effects. Analytical expressions for contact force, contact radius, and contact pressure are derived in explicit forms. Additionally, three sources of nonlinearity—geometric, material, and contact boundary-condition—in the flattening problem are analyzed, revealing that geometric nonlinearity plays a dominant role, while material and contact property nonlinearities have minimal influence.

To address these nonlinearities, correction functions for the contact force (Eq. (38)) and contact radius (Eq. (42)) are proposed in the form of simple linear functions. Notably, the correction function for the contact force depends only on the compression ratio (δ/R) and is independent of Poisson's ratio, whereas the correction function of the contact radius is a function of both the compression ratio and Poisson's ratios. The exact forms of these functions are determined through least-square fitting of the FEA results, yielding explicit expressions for the contact force, contact radius, and contact pressure. The proposed analytical expressions are validated against experimental results using Ecoflex spheres, demonstrating high accuracy and effectiveness within a compression ratio range up to 80 %. Furthermore, the applicability of the solution of the contact force vs. compression ratio to cellular systems is explored, demonstrating good agreements between the model prediction and experimental measurements. This work provides a practical and simplified approach to addressing nonlinearities in the flattening problem, offering valuable insights and tools (e.g., adhesion mechanics (Zhu et al., 2025, 2021) under large deformation) for future studies and applications.

Data availability

All data needed to evaluate the conclusions in the paper are present in the paper and/or the Appendixes. Additional data related to this paper may be requested from the authors.

CRediT authorship contribution statement

Tong Mu: Writing – review & editing, Writing – original draft, Visualization, Validation, Software, Methodology, Investigation, Formal analysis, Data curation. **Ruozhang Li:** Writing – review & editing, Methodology. **Changhong Linghu:** Writing – review & editing, Writing – original draft, Visualization, Validation, Supervision, Software, Project administration, Methodology, Investigation, Formal analysis, Conceptualization. **Yanju Liu:** Writing – review & editing, Supervision, Project administration, Funding acquisition,

Conceptualization. **Jinsong Leng:** Writing – review & editing, Supervision, Project administration, Funding acquisition, Conceptualization. **Huajian Gao:** Writing – review & editing, Writing – original draft, Supervision, Project administration, Methodology, Investigation, Funding acquisition, Formal analysis, Conceptualization. **K. Jimmy Hsia:** Writing – review & editing, Writing – original draft, Visualization, Supervision, Resources, Project administration, Methodology, Investigation, Funding acquisition, Formal analysis, Conceptualization.

Declaration of competing interest

The authors declare that they have no known competing financial interests or personal relationships that could have appeared to influence the work reported in this paper.

Acknowledgements

K.J.H., H.G., and C.L. acknowledge support from the Ministry of Education (MOE) of Singapore under the Academic Research Fund Tier 2 (MOE-T2EP50122–0001). Y.L. and J.L. acknowledges support from the National Key R&D Program of China (2022YFB3805700). T.M. acknowledges support from the China Scholarship Council program (202406120073).

Appendix

A. Solution for the contact force

Substituting Eq. (20) into Eq. (18), the incremental contact force under an infinitesimal displacement increment $d\delta$ is obtained as:

$$dP = \chi\left(\frac{\delta}{R}\right)\cdot 2E^* a_0 d\delta. \tag{A1}$$

Therefore, the contact stiffness is expressed as:

$$\frac{dP}{d\delta} = 2\chi E^* a_0. \tag{A2}$$

Substitute Eq. (25) into Eq. (17) and integrate by parts gives the contact force as:

$$P = 2\chi E^* a_0\delta - 2\chi E^*\int_0^{a_0}\widetilde{\delta}(\widetilde{a}_0)d\widetilde{a}_0. \tag{A3}$$

or,

$$P = 2\chi E^*\int_0^{a_0}[\delta - \widetilde{\delta}(\widetilde{a}_0)]d\widetilde{a}_0. \tag{A4}$$

Under infinite-thickness condition (Eq. (19)), the contact force reduces to the Hertzian contact force:

$$P_{\mathrm{H}} = 2E^*\int_0^{a_0}[\delta - \widetilde{\delta}(\widetilde{a}_0)]d\widetilde{a}_0, \tag{A5}$$

which is expected to equal to Eq. (5) after integrating.

Therefore, the relationship between the contact radius in the intermediate configuration a_0 and the compression displacement satisfies the Hertzian relationship Eq. (2), i.e.,

$$\delta(a_0) = \frac{a_0^2}{R}. \tag{A6}$$

Comparing Eq. (A4) and Eq. (A5), the contact force can be expressed as the product of the correction function and the Hertzian contact force as:

$$P = \chi\left(\frac{\delta}{R}\right)P_{\mathrm{H}}. \tag{A7}$$

B. Constitutive models of elastomers

Elastomeric materials exhibit non-linear elastic mechanical behavior under large deformations, including geometric and material nonlinearity. To capture these phenomena, various constitutive models have been developed. This section provides the formulations of general elastic constitutive model and specific models: neo-Hookean model, Arruda-Boyce model, and Mooney-Rivlin model.

B.1. General concepts

To isolate the volumetric and deviatoric components, the modified deformation gradient is expressed as:

$$\overline{\boldsymbol{F}} = J^{-\frac{1}{3}}\boldsymbol{F}, \tag{B1}$$

then the modified right and left Cauchy-Green tensors are defined as:

$$\overline{\boldsymbol{b}} = \overline{\boldsymbol{F}} \cdot \overline{\boldsymbol{F}}^T, \ \overline{\boldsymbol{C}} = \overline{\boldsymbol{F}}^T \cdot \overline{\boldsymbol{F}}. \tag{B2}$$

To determine the Helmholtz free energy ψ of isotropic elastic materials, the first modified invariant is defined as:

$$\bar{I}_1 = \mathrm{tr}(\overline{\boldsymbol{b}}) = \mathrm{tr}(\overline{\boldsymbol{C}}), \tag{B3}$$

and the second modified invariant is defined as:

$$\bar{I}_2 = \frac{1}{2}\left[\bar{I}_1^2 - tr(\overline{\boldsymbol{b}} \cdot \overline{\boldsymbol{b}})\right] = \frac{1}{2}\left[\bar{I}_1^2 - tr(\overline{\boldsymbol{C}} \cdot \overline{\boldsymbol{C}})\right]. \tag{B4}$$

The PK-1 stress is derived from the derivative of the Helmholtz free energy ψ by:

$$\boldsymbol{T} = \frac{\partial \psi}{\partial \boldsymbol{F}} \tag{B5}$$

thus, the Cauchy stress is obtained from Eq. (12) as:

$$\boldsymbol{\sigma} = \frac{1}{J}\boldsymbol{T} \cdot \boldsymbol{F}^{-T} \tag{B6}$$

In the uniaxial compression, the deformation gradient is written in matrix form as:

$$\boldsymbol{F} = \begin{bmatrix} \lambda_1 & 0 & 0 \\ 0 & \lambda_2 & 0 \\ 0 & 0 & \lambda_3 \end{bmatrix}. \tag{B7}$$

The stretches on the radial direction are equal,

$$\lambda_2 = \lambda_3 = \sqrt{J/\lambda_1}, \tag{B8}$$

and the Cauchy stresses on the radial direction meet,

$$\sigma_2 = \sigma_3 = 0, \tag{B9}$$

or equivalently written by the PK-1 stress,

$$T_2 = T_3 = 0. \tag{B10}$$

The component of the PK-1 stress in the compression direction, T_1, is the compression force:

$$T(\lambda_1) = -T_1, \tag{B11}$$

which is an implicit function of stretch λ_1 determined by Eq. (B5) and Eq. (B10).

B.2. Neo-Hookean model

In the Neo-Hookean model, the Helmholtz free energy of rubbery-like material is only a function of J and $\bar{I}_1$ (Boyce and Arruda, 2000), which can be written as:

$$\psi = W(\bar{I}_1) + U(J), \tag{B12}$$

where W represents the deviatoric energy, and U accounts for volumetric changes. These components are often expressed as polynomial expansions:

$$W = C_{10}(\bar{I}_1 - 3) + C_{20}(\bar{I}_1 - 3)^2 + \cdots, \tag{B13}$$

$$U = \frac{1}{D_1}(J-1)^2 + \frac{1}{D_2}(J-1)^4 + \cdots. \tag{B14}$$

In the small deformation limit, higher-order terms are neglected, leading to the Neo-Hookean model:

$$W = C_{10}(\bar{I}_1 - 3), \tag{B15}$$

$$U = \frac{1}{D_1}(J-1)^2. \tag{A16}$$

The material parameters of the Neo-Hookean model, C_{10} and D_1, are related to the shear modulus μ and Poisson's ratio ν as:

$$C_{10} = \frac{\mu}{2},\ D_1 = \frac{3(1-2\nu)}{(1+\nu)\mu}. \tag{B17}$$

B.3. Arruda-Boyce model

The Arruda-Boyce model is a widely used constitutive framework that accounts for the finite extensibility of polymer chains in rubber-like materials, and effectively predicts the elastic behavior of rubber-like materials over a wide range (Arruda and Boyce, 1993). The Helmholtz free energy of Arruda-Boyce model is:

$$W_{\mathrm{AB}} = \mu\sqrt{n}\left[\beta\lambda_{\mathrm{chain}} + \sqrt{n}\ln\frac{\beta}{\sinh\beta}\right], \tag{B18}$$

where μ is the initial shear modulus, n represents the average number of links in a chain segment, $\lambda_{\mathrm{chain}} = \sqrt{\bar{I}_1/3}$ is the chain stretch ratio, and β is defined as follows:

$$\beta = \mathscr{L}^{-1}\left(\frac{\lambda_{\mathrm{chain}}}{\sqrt{n}}\right), \tag{B19}$$

where $\mathscr{L}^{-1}$ is inverse of Langevin function $\mathscr{L}(x) = \coth x - 1/x$.

The Helmholtz free energy of the Arruda-Boyce model can also be expanded as a polynomial series:

$$W_{\mathrm{AB}} = \mu\left[\frac{1}{2}(\bar{I}_1 - 3) + \frac{1}{20n}(\bar{I}_1^2 - 9) + \frac{11}{1050n^2}(\bar{I}_1^3 - 27) + \frac{19}{7000n^3}(\bar{I}_1^4 - 81) + \frac{519}{673750n^4}(\bar{I}_1^5 - 243) + \cdots\right]. \tag{B20}$$

Meanwhile, the parameter n can be replaced by locking stretch, which is defined as:

$$\lambda_{\mathrm{m}} = \sqrt{n}. \tag{B21}$$

Substituting Eq. (B21) into Eq. (B20), the Helmholtz free energy becomes:

$$W_{\mathrm{AB}} = \mu\left[\frac{1}{2}(\bar{I}_1 - 3) + \frac{1}{20\lambda_{\mathrm{m}}^2}(\bar{I}_1^2 - 9) + \frac{11}{1050\lambda_{\mathrm{m}}^4}(\bar{I}_1^3 - 27) + \frac{19}{7000\lambda_{\mathrm{m}}^6}(\bar{I}_1^4 - 81) + \frac{519}{673750\lambda_{\mathrm{m}}^8}(\bar{I}_1^5 - 243) + \cdots\right]. \tag{B22}$$

B.4. Mooney-Rivlin model

General constitutive models of hyperelastic materials also take account of the influence of the second modified invariant, $\bar{I}_2$. For example, the Mooney-Rivlin model, which has Helmholtz free energy as:

$$W = C_{10}(\bar{I}_1 - 3) + C_{01}(\bar{I}_2 - 3). \tag{B23}$$

When $C_{01} = 0$, Mooney-Rivlin model degenerates into neo-Hookean model.

To meet linear elastic model under small deformations, parameters must meet the requirement as follow:

$$\mu = 2(C_{10} + C_{01}). \tag{B24}$$

The Mooney-Rivlin model, while capable of accurately fitting the mechanical behavior of rubber-like materials within a certain range mathematically, has been shown to exhibit overly stiff behavior in three-dimensional large deformation problems (Boyce and Arruda, 2000). As a result, it is now less commonly used in modeling elastomers. However, for materials such as metals and composites, constitutive models that include the second modified invariant, $\bar{I}_2$, like the Mooney-Rivlin model, still need to be considered.

C. Parameter analysis of material nonlinearity

C.1. Effect on crosslinking density

As the crosslinking density of polymer increases, the parameter n (or equivalently λ_m, as defined in Eq. (B21)) in the Arruda-Boyce model decreases, as discussed in Section B.3. Based on the physical significance of the model, n cannot be <2 for a polymer (i.e., $\lambda_m > 1.4$), which corresponds to each chain segment having at least two links. When $\lambda_m \to \infty$, the Arruda-Boyce model simplifies to the neo-Hookean model. Typical values of λ_m range from 4 to 6 for rubbers (Arruda and Boyce, 1993), SMPs (Nguyen et al., 2008), and hydrogels (You et al., 2023).

Fig. C.1a presents the contact force using the Arruda-Boyce model with various λ_m values of compression ratio δ/R from 0 to 0.5. When $\lambda_m \geq 4$, the deviation remains relatively minimal from the neo-Hookean model. Therefore, the influence of λ_m is negligible for common polymers. However, deviations from the neo-Hookean model become noticeable for results of $\lambda_m \leq 3$ when compression ratio $\delta/R > 0.3$, meaning that material nonlinearity in the flattening problem should be taken into account for very stiff polymers.

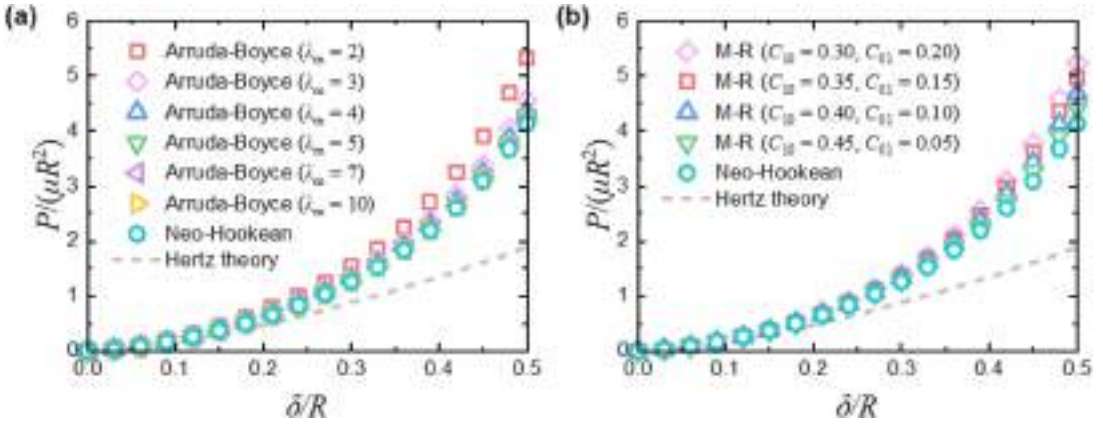

Fig. C.1. Influence of material parameters in common hyperelastic models on the contact force under extreme compressions. (**a**) Comparison of contact forces from FEA simulations using the Arruda-Boyce model with varying parameters λ_m. Results from the neo-Hookean model (green circles), equivalent to the Arruda-Boyce model with $\lambda_m = \infty$ are included for comparison. (**b**) Comparison of contact forces obtained from FEA simulations using the Mooney-Rivlin (M-R) model with different model parameter sets. The Mooney-Rivlin model reduces to the neo-Hookean model when $C_{10} = 0.50$ and $C_{01} = 0$ (green circles). Predictions from the proposed theory (orange solid line) and Hertz model (gray dashed line) are also shown for reference.

C.2. Effect of second invariant

When the constitutive model considers the second modified invariant, $\bar{I}_2$, such as in the Mooney-Rivlin model (refer to Appendix B.4), mechanical behavior under extreme deformations becomes sensitive to the constitutive model of materials. This section investigates the influence of the parameter C_{01} on the flattening problem using FEA. The initial shear modulus is fixed at 1 MPa, with C_{10} varying from 0.3 to 0.5, and C_{01} is determined using Eq. (B24). The contact force results calculated with different model parameters are shown in Fig. C.1b

The results indicate that when the compression ratio $\delta/R \leq 0.3$, the FEA results show no significant difference between different parameter sets. However, when $\delta/R > 0.3$, the results calculated using $C_{01} > 0$ deviate increasingly from those obtained using the neo-Hookean model ($C_{01} = 0$) as δ/R increases. Moreover, the deviation shows a linear correlation with the value of C_{01}.

Although the second modified invariant significantly impacts the flattening problem under extreme deformation, $C_{01}/C_{10} < 0.1$ is typical for rubber-like elastomers (Boyce and Arruda, 2000). Thus, insensitivity of material nonlinearity under extreme deformation can generally be maintained for elastomers. However, if the second modified invariant contributes substantially to the material's Helmholtz free energy, it is necessary to consider material nonlinearity in flattening problem.

D. Preparation of Ecoflex spheres

The Ecoflex samples were prepared following the below steps: First, the A and B components of Ecoflex 00-30 was thoroughly mixed in the baker using a glass rod and degassed in a vacuum oven to remove air bubbles. Then, the mixture was then injected into a spherical mold with diameter of 10 mm and subjected to another round of evacuation to eliminate bubbles formed in injection process. After resting for 5 h at room temperature, the Ecoflex 00-30 sphere was cured and demolded for testing.

E. Strain analysis of the flattening problem

To explain the observed similarity between our model predictions and that of the neo-Hookean and Arruda-Boyce models in Fig. 5,

we examine the principal true strain within in the flattening problem during compression. Fig. E.1 illustrates the maximum value of the maximum principal true strain (in absolute value) in an elastic sphere under a certain compression ratio. When compression ratio of $\delta/R \leq 0.5$, the absolute value of the maximum true strain in the sphere does not exceed 1. At these strain levels, the nonlinear effects of the material remain negligible (also see the inset in Fig. 5a. FEA results also indicate that the distributions of the maximum principal strain (in absolute terms) are nearly identical when using the neo-Hookean model and the Arruda-Boyce model ($\lambda_m = 5$).

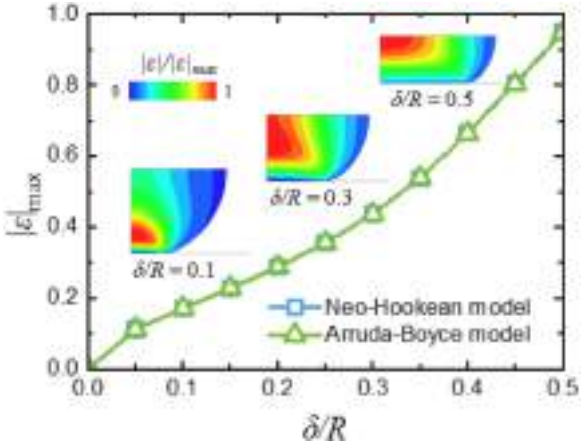

Fig. E.1. FEA simulation results of the maximum principal true strain (absolute value) in the elastic sphere under extreme compression. Inserts show the distributions of the maximum in-plane principal true strain (absolute value) of a neo-Hookean material sphere at compression ratios of 0.1, 0.3, and 0.5.

F. Validation of Force-Contact Radius Predictions

To further validate the proposed contact model, we evaluate the contact force vs. the contact radius for the flattening problem of an incompressible neo-Hookean material. The predictions from the proposed model (obtained by solving Eqs. (24), (27), and (37)) are compared with FEA results and the classical Hertz theory, as shown in Fig. F.1. The figure shows that while Hertz theory agrees well with FEA results at small deformations, it underestimates the contact force as the contact radius $a/R > 1.5$. In contrast, the proposed model maintains excellent agreement with FEA results across the full deformation range, including under conditions of extreme flattening.

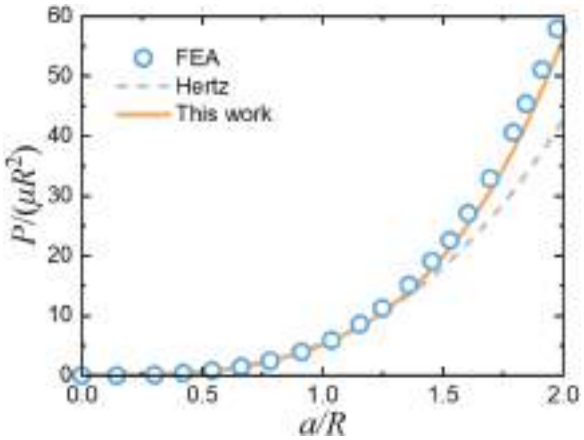

Fig. F.1. Comparison of predicted contact force versus contact radius curves for the flattening problem obtained from the proposed model (this work, orange solid line) and Hertz theory (gray dashed line), validated against the FEA results (blue circles). FEA simulations were performed with $R = 1$ mm, $\mu = 1$ MPa, and $\nu = 0.5$.

References

Abondance, S., Teeple, C.B., Wood, R.J., 2020. A dexterous soft robotic hand for delicate in-hand manipulation. IEEE Robot. Autom. Lett. 5, 5502–5509.
Arruda, E.M., Boyce, M.C., 1993. A three-dimensional constitutive model for the large stretch behavior of rubber elastic materials. J. Mech. Phys. Solids 41, 389–412.
Aymard, A., Delplanque, E., Dalmas, D., Scheibert, J., 2024. Designing metainterfaces with specified friction laws. Science 383, 200–204.

Boyce, M.C., Arruda, E.M., 2000. Constitutive models of rubber elasticity: a review. Rubber Chem. Technol. 73, 504–523.
Chen, P., Chen, S., 2013. Partial slip contact between a rigid punch with an arbitrary tip-shape and an elastic graded solid with a finite thickness. Mech. Mater. 59, 24–35.
Chen, S., Gao, H., 2007. Bio-inspired mechanics of reversible adhesion: orientation-dependent adhesion strength for non-slipping adhesive contact with transversely isotropic elastic materials. J. Mech. Phys. Solids 55, 1001–1015.
Chen, Y.-C., Lagoudas, D.C., 2008. A constitutive theory for shape memory polymers. part I: large deformations. J. Mech. Phys. Solids 56, 1752–1765.
Choi, C., Schwarting, W., DelPreto, J., Rus, D., 2018. Learning object grasping for soft robot hands. IEEE Robot. Autom. Lett. 3, 2370–2377.
Dassault Systèmes, 2023. Abaqus user manual.
Diani, J., Liu, Y., Gall, K., 2006. Finite strain 3D thermoviscoelastic constitutive model for shape memory polymers. Polym. Eng. Sci. 46, 486–492.
Du, Y., Stewart, P., Hill, N.A., Yin, H., Penta, R., Köry, J., Luo, X., Ogden, R., 2023. Nonlinear indentation of second-order hyperelastic materials. J. Mech. Phys. Solids 171, 105139.
Fakhouri, S., Hutchens, S.B., Crosby, A.J., 2015. Puncture mechanics of soft solids. Soft Matter 11, 4723–4730.
Flavin, M.T., Ha, K.-H., Guo, Z., Li, S., Kim, J.-T., Saxena, T., Simatos, D., Al-Najjar, F., Mao, Y., Bandapalli, S., Fan, C., Bai, D., Zhang, Z., Zhang, Y., Flavin, E., Madsen, K.E., Huang, Y., Emu, L., Zhao, J., Yoo, J.-Y., Park, M., Shin, J., Huang, A.G., Shin, H.-S., Colgate, J.E., Huang, Y., Xie, Z., Jiang, H., Rogers, J.A., 2024. Bioelastic state recovery for haptic sensory substitution. Nature 635, 345–352.
Fregonese, S., Bacca, M., 2021. Piercing soft solids: a mechanical theory for needle insertion. J. Mech. Phys. Solids 154, 104497.
Gao, H., Wang, X., Yao, H., Gorb, S., Arzt, E., 2005. Mechanics of hierarchical adhesion structures of geckos. Mech. Mater. 37, 275–285.
Ghaednia, H., Wang, X., Saha, S., Xu, Y., Sharma, A., Jackson, R.L., 2017. A review of elastic–plastic contact mechanics. Appl. Mech. Rev. 69.
Guo, Z., Lyu, Q., Jiang, L., Chen, Y., Dong, L., Zhang, H., 2020. Contact model for incompressible neo-hookean materials under finite spherical indentation. J. Appl. Mech. 87.
Herren, B., Saha, M.C., Altan, M.C., Liu, Y., 2020. Development of ultrastretchable and skin attachable nanocomposites for human motion monitoring via embedded 3D printing. Compos. B: Eng. 200, 108224.
Hertz, H., 1882. Ueber die Berührung fester elastischer Körper. J. Reine Angew. Math. 1882, 156–171.
Hong, W., Liu, Z., Suo, Z., 2009. Inhomogeneous swelling of a gel in equilibrium with a solvent and mechanical load. Int. J. Solids Struct. 46, 3282–3289.
Huang, R., Zheng, S., Liu, Z., Ng, T.Y., 2020. Recent advances of the constitutive models of smart materials — hydrogels and shape memory polymers. Int. J. Appl. Mech. 12, 2050014.
Hui, C.-Y., Wu, H., Jagota, A., Khripin, C., 2021. Friction force during lubricated steady sliding of a rigid cylinder on a viscoelastic substrate. Tribol. Lett. 69, 30.
Lachhab, T., Weill, C., 1999. Compression of a soft sphere packing. Eur. Phys. J. B-Condens. Matter Complex Syst. 9, 59–69.
Leng, H., Lin, Y., 2011. From human skin to nano-skin: an experimental study on human skin temperature measurement. Int. J. Smart Nano Mater. 2, 78–91.
Li, C., Luo, H., Lin, X., Zhang, S., Song, J., 2024a. Laser-driven noncontact bubble transfer printing via a hydrogel composite stamp. Proc. Natl. Acad. Sci. 121, e2318739121.
Li, C., Zhang, S., Jiang, J., Wang, S., He, S., Song, J., 2024b. Laser-induced adhesives with excellent adhesion enhancement and reduction capabilities for transfer printing of microchips. Sci. Adv. 10, eads9226.
Li, S., Wu, J., Peng, X., Feng, X.-Q., 2024c. Unlocking the potential of transdermal drug delivery. Int. J. Smart Nano Mater. 15, 432–468.
Li, X., Peng, Z., Yang, Y., Chen, S., 2018. Tunable adhesion of a bio-inspired micropillar arrayed surface actuated by a magnetic field. J. Appl. Mech. 86.
Linghu, C., Liu, Y., Tan, Y.Y., Sing, J.H.M., Tang, Y., Zhou, A., Wang, X., Li, D., Gao, H., Hsia, K.J., 2023a. Overcoming the adhesion paradox and switchability conflict on rough surfaces with shape-memory polymers. Proc. Natl. Acad. Sci. 120, e2221049120.
Linghu, C., Mu, T., Zhao, W., Liu, Y., Hsia, K.J., Leng, J., Gao, H., 2024. Advancing smart dry adhesives with shape memory polymers. Int. J. Smart Nano Mater. 1–41.
Linghu, C., Yang, X., Liu, Y., Li, D., Gao, H., Hsia, K.J., 2023b. Mechanics of shape-locking-governed R2G adhesion with shape memory polymers. J. Mech. Phys. Solids 170, 105091.
Liu, K.K., Williams, D.R., Briscoe, B.J., 1998. The large deformation of a single micro-elastomeric sphere. J. Phys. D Appl. Phys. 31, 294.
Lulevich, V., Zink, T., Chen, H.-Y., Liu, F.-T., Liu, G.-y., 2006. Cell mechanics using atomic force microscopy-based single-cell compression. Langmuir 22, 8151–8155.
McGarry, J.P., 2009. Characterization of cell mechanical properties by computational modeling of parallel plate compression. Ann. Biomed. Eng. 37, 2317–2325.
Mo, Y., Turner, K.T., Szlufarska, I., 2009. Friction laws at the nanoscale. Nature 457, 1116–1119.
Moeendarbary, E., Harris, A.R., 2014. Cell mechanics: principles, practices, and prospects. WIREs Syst. Biol. Med. 6, 371–388.
Moore, S.W., Manzari, M.T., Shen, Y.-L., 2010. Nanoindentation in elastoplastic materials: insights from numerical simulations. Int. J. Smart Nano Mater. 1, 95–114.
Mott, P.H., Dorgan, J.R., Roland, C.M., 2008. The bulk modulus and Poisson's ratio of "incompressible" materials. J. Sound Vib. 312, 572–575.
Nguyen, T.D., Jerry Qi, H., Castro, F., Long, K.N., 2008. A thermoviscoelastic model for amorphous shape memory polymers: incorporating structural and stress relaxation. J. Mech. Phys. Solids 56, 2792–2814.
Park, K., Millet, L.J., Kim, N., Li, H., Jin, X., Popescu, G., Aluru, N.R., Hsia, K.J., Bashir, R., 2010. Measurement of adherent cell mass and growth. Proc. Natl. Acad. Sci. 107, 20691–20696.
Popov, V.L., Heß, M., Willert, E., 2019. Handbook of Contact mechanics: Exact Solutions of Axisymmetric Contact Problems. Springer Nature.
Segedin, C.M., 1957. The relation between load and penetration for a spherical punch. Mathematika 4, 156–161.
Shi, X., Liu, Z., Feng, L., Zhao, T., Hui, C.-Y., Zhang, S., 2022. Elastocapillarity at cell-matrix contacts. Phys. Rev. X 12, 021053.
Sneddon, I.N., 1965. The relation between load and penetration in the axisymmetric boussinesq problem for a punch of arbitrary profile. Int. J. Eng. Sci. 3, 47–57.
Tartibi, M., Liu, Y.X., Liu, G.Y., Komvopoulos, K., 2015. Single-cell mechanics – an experimental–computational method for quantifying the membrane–cytoskeleton elasticity of cells. Acta Biomater. 27, 224–235.
Tatara, Y., 1991. On compression of rubber elastic sphere over a large range of displacements—part 1: theoretical study. J. Eng. Mater. Technol. 113, 285–291.
Tatara, Y., Shima, S., Lucero, J.C., 1991. On compression of rubber elastic sphere over a large range of displacements—part 2: comparison of theory and experiment. J. Eng. Mater. Technol. 113, 292–295.
Tee, B.C.-K., Chortos, A., Berndt, A., Nguyen, A.K., Tom, A., McGuire, A., Lin, Z.C., Tien, K., Bae, W.-G., Wang, H., Mei, P., Chou, H.-H., Cui, B., Deisseroth, K., Ng, T. N., Bao, Z., 2015. A skin-inspired organic digital mechanoreceptor. Science 350, 313–316.
Theocaris, P.S., 1969. Interrelation between dynamic moduli and compliances in polymers. Kolloid-Z. Z. Polym. 235, 1182–1188.
Treloar, L.G., 1975. The physics of rubber elasticity.
Xiao, S., Peng, Z., Wu, H., Yao, Y., Chen, S., 2023. Surface effect in nano-scale fretting contact problems. J. Appl. Mech. 90.
Xydas, N., Kao, I., 1999. Modeling of contact mechanics and friction limit surfaces for soft fingers in robotics, with experimental results. Int. J. Rob. Res. 18, 941–950.
Yang, T., Deng, W., Chu, X., Wang, X., Hu, Y., Fan, X., Song, J., Gao, Y., Zhang, B., Tian, G., Xiong, D., Zhong, S., Tang, L., Hu, Y., Yang, W., 2021. Hierarchically microstructure-bioinspired flexible Piezoresistive bioelectronics. ACS Nano 15, 11555–11563.
You, H., Zheng, S., Lam, K.Y., Li, H., 2023. From loop probability of self-avoiding walk to constitutive models of hydrogels for thickness, strain-softening and hardening effects. Extreme Mech. Lett. 64, 102083.
Yu, C., Zeng, W., Wang, B., Cui, X., Gao, Z., Yin, J., Liu, L., Wei, X., Wei, Y., Dai, Z., 2025. Stiffer is stickier: adhesion in elastic nanofilms. Nano Lett. 25, 1876–1882.
Zhang, J., Yao, H., Mo, J., Chen, S., Xie, Y., Ma, S., Chen, R., Luo, T., Ling, W., Qin, L., Wang, Z., Zhou, W., 2022. Finger-inspired rigid-soft hybrid tactile sensor with superior sensitivity at high frequency. Nat. Commun. 13, 5076.
Zhang, T., 2023. Mechanics of tunable adhesion with surface wrinkles. J. Appl. Mech. 90.
Zhao, J., Li, X., Tan, Y., Liu, X., Lu, T., Shi, M., 2022. Smart adhesives via magnetic actuation. Adv. Mater. 34, 2107748.
Zheng, Z., Yu, J., 2007. Using the Dugdale approximation to match a specific interaction in the adhesive contact of elastic objects. J. Colloid Interface Sci. 310, 27–34.
Zhi-Jun Zheng, J.Y., 2007. A generalized maugis model for adhesive contact of arbitrary axisymmetric elastic objects. Chin. J. Theor. Appl. Mech. 23, 382–388.

Zhu, H., Luo, H., Cai, M., Song, J., 2024. A multifunctional flexible tactile sensor based on resistive effect for simultaneous sensing of pressure and temperature. Adv. Sci. 11, 2307693.
Zhu, Y., Ni, Y., Huang, C., Yu, J., Yao, H., Zheng, Z., 2025. Unified model for adhesive contact between solid surfaces at micro/nano-scale. J. Mech. Phys. Solids 196, 106004.
Zhu, Y., Zheng, Z., Zhang, Y., Wu, H., Yu, J., 2021. Adhesion of elastic wavy surfaces: interface strengthening/weakening and mode transition mechanisms. J. Mech. Phys. Solids 151, 104402.